nature nanotechnology

Article

https://doi.org/10.1038/s41565-023-01439-7

Precise electrokinetic position and three-dimensional orientation control of a nanowire bioprobe in solution

Received: 26 October 2022

Accepted: 1 June 2023

Published online: 27 July 2023



Check for updates

Huaizhi Li 1, Daniel Teal 2, Zexi Liang, Hyunah Kwon 3,4, David Huo,5, Alison Jin⁶, Peer Fischer^{3,4} & Donglei Emma Fan © ^{1,2}

Owing to Brownian-motion effects, the precise manipulation of individual micro- and nanoparticles in solution is challenging. Therefore, scanning-probe-based techniques, such as atomic force microscopy, attach particles to cantilevers to enable their use as nanoprobes. Here we demonstrate a versatile electrokinetic trap that simultaneously controls the two-dimensional position with a precision of 20 nm and 0.5° in the three-dimensional orientation of an untethered nanowire, as small as 300 nm in length, under an optical microscope. The method permits the active transport of nanowires with a speed-dependent accuracy reaching 90 nm at 2.7 µm s⁻¹. It also allows for their synchronous three-dimensional alignment and rotation during translocation along complex trajectories. We use the electrokinetic trap to accurately move a nanoprobe and stably position it on the surface of a single bacterial cell for sensing secreted metabolites for extended periods. The precision-controlled manipulation underpins developing nanorobotic tools for assembly, micromanipulation and biological measurements with subcellular resolution.

Recent advances in the understanding and exploration of active matter, micro-/nanomachines and microrobots suggest their potential biomedical applications¹⁻⁷. One promising direction is to use microand nanostructures as probes or to locally exert forces. To manipulate and control individual nanostructures with subcellular precision is challenging due to the presence of strong Brownian forces. Schemes that can manipulate untethered probes are largely restricted to two dimensions and cannot be used to freely orient an untethered micro-/ nanoprobe. Therefore, most probes are attached to a cantilever^{8,9}.

Optical¹⁰⁻¹⁴, magnetic¹⁵⁻²⁰, hydrodynamic²¹⁻²⁴, acoustic^{25,26} and thermophoretic²⁷ tweezers permit the two-dimensional (2D) positioning of micro-/nanoscale particles, cells and micro-objects. This enables a wide range of applications ranging from non-invasive spectroscopic $observations \, to \, force \, measurements^{15,28,29}. \, Electric \, fields^{30-35} \, have \, also \,$ been used for trapping and manipulation, and they are currently able to trap some of the smallest particles, including molecules³⁶. This is achieved by the judicious application of electric fields that control fluid flows under feedback to counter any Brownian motion of the trapped particle/molecule. The technique is known as an anti-Brownian electrophoretic trap 36,37 . Although the aforementioned traps can be used to position objects, very few techniques can be used to simultaneously control the position of an object and its orientation in space (Supplementary Table 1)14,18,22,24,33,38,39.

Here we report a versatile method to simultaneously control the 2D position and three-dimensional (3D) orientation of micro-/ nanoscale wires, rods and complex anisotropic structures in solution

¹Materials Science and Engineering Program, Texas Materials Institute, University of Texas at Austin, Austin, TX, USA: ²Walker Department of Mechanical Engineering, University of Texas at Austin, Austin, TX, USA. 3Institute for Molecular Systems Engineering and Advanced Materials, Heidelberg University, Heidelberg, Germany. ⁴Max Planck Institute for Medical Research, Heidelberg, Germany. ⁵Department of Biomedical Engineering, University of Texas at Austin, Austin, TX, USA. 6Chandra Family Department of Electrical and Computer Engineering, University of Texas at Austin, Austin, TX, USA. e-mail: dfan@austin.utexas.edu

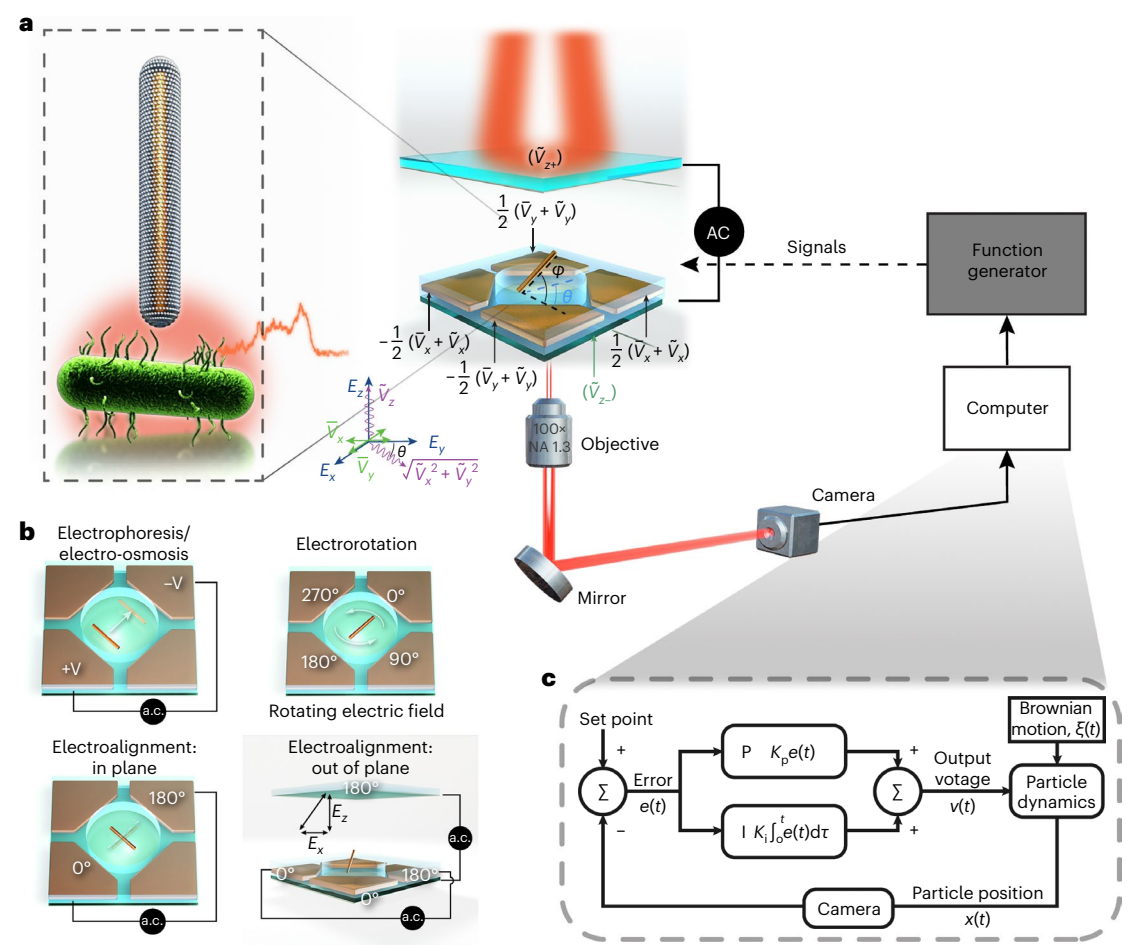


Fig. 1 | **Design and working principle of the electrokinetic trap. a**, Schematic of the electrokinetic trap and the experimental setup to control the position and 3D orientation of a nanoprobe. The inset shows the precise positioning of a plasmonic nanoprobe for the localized detection of metabolites released by a

single bacterial cell. $\bf b$, Electrokinetic effects, including electrophoresis/electrosmosis and in-plane and out-of-plane electroalignment for transport and orientation. $\bf c$, Anti-Brownian-motion manipulation based on a PI algorithm.

with high precision and countering both translational and rotational Brownian motion. Electric fields are applied to utilize electro-osmotic and electrophoretic effects, as well as electrorotation and electroalignment to simultaneously achieve 2D transport, rotation and 3D alignment of the particle with complete position and orientation control.

Figure 1a shows the scheme of the electrokinetic trap to control a free nanowire in solution (Methods). We would like to stress that the surfaces of the observation chamber are not needed to orient the nanowire probe. The trap is formed by four in-plane electrodes and a pair of electrodes orthogonal to the plane to ensure that their combined electric-field vector can point in all three spatial directions, namely, *X*, *Y* and *Z* (Fig. 1a,b). The application of d.c. fields gives rise to electro-osmosis and electrophoresis that causes a nanowire or rod-shaped particle to translate, whereas the application of an a.c. field induces electrorotation or electroalignment, which can be used for the orientation (Fig. 1b). Incorporating a visual feedback mechanism permits anti-Brownian-motion control in all these discussed manipulations (Fig. 1c). Figure 1a (inset) shows a nanowire probe that is steered along a bacterial cell for chemical sensing.

Working principle and experimental design

Several electrokinetic effects have been explored for manipulating micro-/nanoparticles 40 . The applied electric force and torque can be substantial. For instance, electro-osmotic flows can reach velocities of a few millimetres per second and can propel a particle 37 . The torque can be used to spin a nanowire at 18,000 revolutions per minute 41 .

The low-Reynolds-number conditions ensure that the particles respond instantaneously, even when the fields are switched within microseconds. Importantly, electric forces and torques generated via different mechanisms can be readily superimposed by generating suitable electric driving signals (Supplementary Fig. 1). This is exploited in this work, where we achieve combined programmed 3D orientation, continuous rotation and 2D position control of a nanowire (Supplementary Fig. 2). Independent feedback loops further counter the particle's translational and rotational Brownian motion at the same time (Fig. 1c).

Figure 1a shows that d.c. voltages cause the transport of nanoparticles suspended in the polydimethylsiloxane (PDMS) well via electro-osmosis/electrophoresis, which is described by the Helmholtz–Smoluchowski equation under the assumption of a thin double layer⁴², given by $u=-\frac{\epsilon\zeta_s E}{\eta}$ and $U=\frac{\epsilon\zeta_p E}{\eta}$, respectively, where u is the velocity of the electro-osmotic flow; U is the velocity of the particle; ε is the permittivity of the medium; ζ_s and ζ_p are the zeta potentials of the substrate and particle, respectively; η is the viscosity of the medium; and E is the electric-field strength.

Electrorotation (τ_R) , expressed as $\tau_R = -\frac{E^2}{2} \text{Im}[\alpha_a + \alpha_b]$, is achieved by applying a.c. voltages with 90° sequential phase shift that rotate particles 40,43 , where α_a and α_b are the complex polarizabilities along the long axis (a) and short axis (b) of the particle, respectively; both Maxwell–Wagner interfacial polarization and the presence of an electric double layer can contribute to the complex polarizabilities 43 .

As an asynchronous effect, electrorotation supports high-speed spinning and rapid orientation⁴¹.

Electroalignment ($\tau_{\rm A}$) can be obtained from torques generated due to interactions between the high-frequency a.c. electric fields and a polarized particle^{40,44}, as calculated by $\tau_{\rm A} = \frac{\ell^2}{2} {\rm Re}[\alpha_a - \alpha_b] {\rm cos}\theta {\rm sin}\theta$,

where θ is the angle between the electric field and the particle's long axis. In-plane alignment of a nanowire can be readily achieved by applying a simple a.c. electric field in the desired X-Y direction. However, the controlled alignment of nanowires along any desired angle in 3D space, which is essential for nanowire probes, has not yet been realized with electric manipulation. It is because the orientation in space also requires control of the vertical electric field that passes through two dielectric media, which alters the electric-field distribution in the Z direction. Here we apply an equivalent circuit that accounts for the different dielectric layers with a virtual ground voltage set at the nanomanipulation plane to compute the required voltages on the Zelectrodes. Although a simple a.c. field in the Z direction can align the nanowires vertically⁴⁵, this alignment is affected by the in-plane electrodes in all the regions but the very centre of the trap. Thus, such a simple design cannot be used to orient a nanowire in three dimensions, and the driving scheme developed here becomes necessary (Supplementary Note 1 and Supplementary Video 1 show examples). The fields can, thus, be applied either simultaneously or sequentially to achieve the respective transport, 3D alignment and rotation, as well as their combinations.

According to Earnshaw's theorem, it is not possible to achieve a stable electric potential trap for a charged particle⁴⁶. It, thus, becomes necessary to constantly counter the passive Brownian motion by inducing active motion and hence the term electrokinetic trap. We, therefore, apply a vision-based voltage-feedback algorithm for simultaneously countering the particle's translational and rotational Brownian motion. Specifically, the location and orientation of a particle obtained from a camera with image processing based on a minimized rectangular contour are fed to a proportional-integral (PI) control algorithm (Methods and Supplementary Note 2). The necessary electric fields (voltages) are computed and applied to generate force and torque for anti-Brownian-motion control with the same mechanisms for propulsion and rotation (Supplementary Note 3). Here we optimize the PI control algorithm by tuning $K_{\rm p}$ and K_i , which are the gains of the proportional (P) and integral (I) terms. respectively. For angle control, the Palgorithm is also utilized. Both optimizations follow the Ziegler-Nichols method (Supplementary Note 4).

Position control

As shown in Fig. 2a–c, a nanowire is stably trapped at the designated target position (Fig. 2c), with PI control countering the Brownian motion. The random displacement from the target follows a Gaussian distribution (Fig. 2b, inset), with a precision (σ) of 70 nm for a 4-µm-long nanowire (170 nm in diameter) and the averaged position coinciding with the target. With further simultaneous orientation control, the precision in position reaches 56 ± 6 nm for 6.4-µm-long nanowires aligned transversely. The precision increases with the length of the nanowire from 151 ± 22 nm (length, 0.8 µm) to 75 ± 13 nm (6.4 µm), and from 133 ± 22 nm (0.8 µm) to 56 ± 6 nm (6.4 µm) in the parallel and transverse directions, respectively (Fig. 2d). The observed increase in control precision with length (L) can be understood from a particle's Brownian-motion displacement given by $d = \sqrt{\frac{2D}{f}}$ in a frame of the camera recording (1/f), which determines the limit in the precision of a feedback-controlled position. Here D is the translational diffusion

coefficient and f is the camera's operation frequency. For anisotropic

cylindrical nanoparticles, Brownian motion is described by the diffu-

sion coefficients D_a and D_b (Supplementary Note 5)^{35,36}:

$$D_a = \frac{k_{\rm B}T}{2\pi\eta L}(\delta - \gamma_a),\tag{1}$$

$$D_b = \frac{k_{\rm B}T}{4\pi\eta L}(\delta - \gamma_b),\tag{2}$$

which are along the long (a) and short (b) axes, respectively, where k_B , T and $(\delta - \gamma_a)$ and $(\delta - \gamma_b)$ are the Boltzmann constant, temperature in Kelvin, and shape factors that depend only on the aspect ratio, respectively; also, $\delta = \ln\left(\frac{2l}{d}\right)$. Here D_a is always greater than D_b from the above equations (Supplementary Fig. 3a). Correspondingly, the positioning along the transverse direction is more accurate as it shows less Brownian motion, as $D_b < D_a$ (Fig. 2d). The orientation effect is clearly shown in Fig. 2e, where the precision along the X axis (σ_x) (blue) steadily improves when a nanowire orients its long axis from parallel (0°) to transverse (90°) to the X axis and vice versa for σ_v (orange).

We find that when the length of a wire is reduced to 2 μ m, the positioning becomes less angle dependent (Fig. 2d). At this length, the out-of-plane motion of a nanowire increases substantially compared with that of a long nanowire, which makes the video-based feedback more difficult. We overcome this by applying a linear a.c. electric field (50 V_{pp}). The precision still reaches 133 ± 22 nm and 151 ± 22 nm in the transverse and parallel orientations, respectively, for a 0.8- μ m-long wire (Fig. 2d). Indeed, in deionized water, the designed electric trap can successfully trap and align nanowires as small as 0.8 μ m in length.

In-plane orientation control

A nanowire's rotational Brownian motion follows $\langle \Delta\theta^2(t)\rangle=2D_Rt$ (ref. 47). We use PI control based on either electrorotation or 45° electroalignment, which successfully controls the angular position (Fig. 3a,b). Similar to the manipulation of position, the histogram of angular displacement follows a Gaussian distribution with the standard deviation (s.d.) denoted by σ , and the averaged position coinciding with the target angle (Fig. 3b (inset) shows the electrorotation). Similar to translational diffusivity, rotational diffusivity reduces for a longer nanowire following the Broersma relation 48 (Fig. 3c). The precision increases with the length and reaches $1.75\pm0.06^\circ$ and $1.78\pm0.13^\circ$ with electroalignment and electrorotation PI algorithms for 6.4-µm-long nanowires, respectively (Fig. 3d).

Although the application of a linear a.c. field can align a nanowire, the torque approaches zero as the target angle is approached. The rotation is, thus, correspondingly slow and liable to Brownian-motion deviations. For instance, it takes 52 ms for a linear a.c. electric field at 40 $V_{\rm pp}$ (500 kHz) to orient a rod (4 μ m in length and 170 nm in diameter) by 75°. Moreover, the feedback-controlled electrorotation or electroalignment field at only 10 $V_{\rm pp}$ just takes 25 and 38 ms, respectively (Supplementary Note 4). Feedback indeed makes for faster reorientation and requires a much lower voltage (Fig. 3e).

Out-of-plane orientation control is achieved with an a.c. field along the Z direction. The angle can be set between 0 to 90° by tuning the ratio of the in-plane and vertical in-phase electric fields (Fig. 3f). Experimentally, we obtain a series of altitude angles (φ ; Fig. 1) guided by theoretical predictions (Supplementary Video 2 and Supplementary Note 6). This capability is necessary for high-resolution tip-based pattern writing, biomanipulation and sensing operations.

The manipulation precisions are statistically determined (Methods). The results measured at 25 locations across a 117 μ m × 117 μ m area, 62% of the field of view of a 40× objective, are consistent. The s.d. values are 6 nm, 3 nm and 0.1° for σ_a , σ_b and σ_θ , respectively (Supplementary Note 7).

Strength of the electrokinetic trap

The precisions in both positioning and orientation can be improved by increasing the video-tracking frame rate (we use up to 850 frames

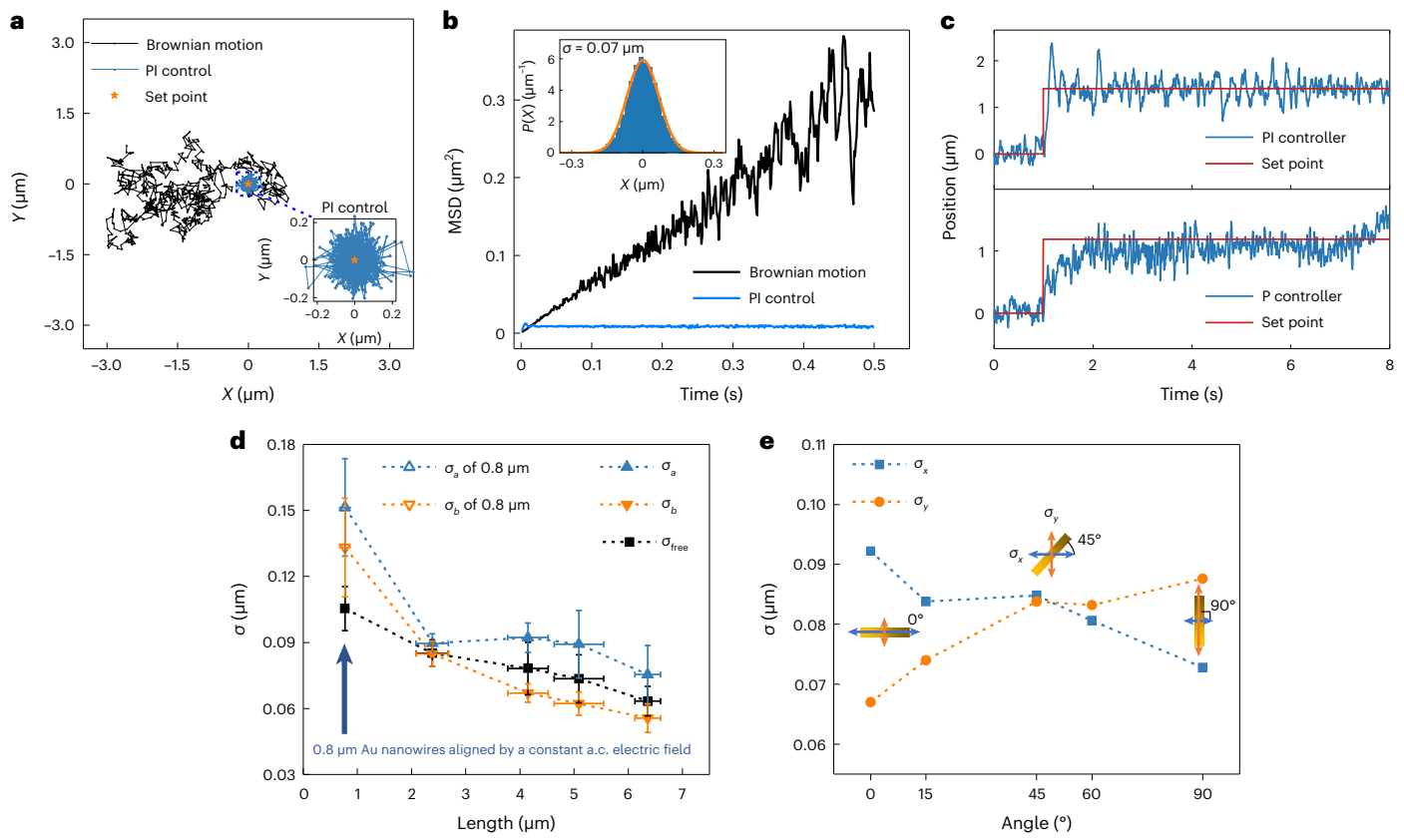


Fig. 2 | **Angle-dependent precise manipulation. a, b,** Two-dimensional displacement (**a**) and time-dependent positional mean-square displacement (MSD) of nanowires in deionized water (**b**). Brownian motion (black line) and under PI control (blue) are also indicated. The inset in **b** shows a histogram of displacement under PI control with a Gaussian fit (orange). **c**, PI control performance (top): position versus time of a nanowire moving to a new set point. The nanowire is trapped at the exact target position compared with that of the P control (bottom) (160 fps; P control, $K_p = 0.077$; PI control, $K_p = 0.06$, $K_i = 1.66$). **d**, Precision in the position of aligned nanowires of various lengths along their long (σ_a) and short (σ_b) axes and the non-aligned value (σ_{free}). The alignment

of nanowires is achieved via electrorotation P control. The $0.8~\mu m$ nanowire is oriented via a linear 50 V_{pp} , 500 kHz a.c. electric field. The horizontal and vertical error bars represent the s.d. values of the length and precision measured from five different nanowires, respectively. \boldsymbol{e} , Precision of position control of Au nanowires (4 μm in length; multiple wires) along the X (σ_{x} , blue) and Y (σ_{y} , orange) axes, aligned at a series of angles (Supplementary Fig. 7 shows the error bars), systematically confirms the enhanced manipulation precision along the short axis of a longitudinal nanostructure. The dashed lines in \boldsymbol{d} and \boldsymbol{e} are guides to the eye. Data are presented as mean values \pm s.d. Five nanowires are measured to derive the statistics in \boldsymbol{d} and \boldsymbol{e} .

per second (fps)) (Fig. 3g) or by increasing the viscosity (Fig. 3i). Interestingly, the particle's surface charge also influences the precision of the in-plane manipulation. Native Au nanowires and a glass substrate are both negatively charged in deionized water. As a result, the propulsion forces due to electro-osmosis and electrophoresis point in opposite directions. It is, thus, advantageous to modify the surface of the Au nanowires with positively charged polyelectrolytes (Methods). This charge reversal ensures that the electrophoretic and electro-osmotic forces point in the same direction as that of the electric field. This enhances the propulsion force and thus boosts the average speed of the Au nanowires. For our experimental conditions, we find an increase in speed from 6.2 to 15.2 μm s⁻¹ (Supplementary Fig. 4) coupled with an increase in the positioning precision from 152 ± 7 to 137 ± 9 nm (Fig. 3h). Similarly, the surface charge of the substrate affects the flow speeds (Supplementary Fig. 4). The PI control performance is positively correlated with the restoring force of the trap; the higher the strength of the trap, the better is the precision. However, surface treatment had little effect on the torques of electroalignment or electrorotation and thus the angular precision, which can be attributed to their governance by electric polarizability.

We determine the spring constants of the trap given by $k = \frac{k_B I}{o^2}$, for the long (L) and short (S) directions of an in-plane nanowire, and along an in-plane direction for a vertically aligned nanowire (V)

in a glycerol:water mixture (3:1) (Fig. 3i) as $k_{\rm L} = 3.2 \times 10^{-6}$ N m⁻¹, $k_{\rm S} = 9.3 \times 10^{-6}$ N m⁻¹ and $k_{\rm V} = 4.3 \times 10^{-6}$ N m⁻¹, as well as the corresponding precision in the spatial dimensions of 36 ± 6 , 21 ± 3 and 31 ± 5 nm, respectively. The nanowires can also be oriented with a high precision of $0.51 \pm 0.04^{\circ}$ in plane with a corresponding torsional trap constant $k_{\rm R} = 5.2 \times 10^{-17}$ N m rad⁻¹.

Evidently, the in-plane manipulation of a vertical nanowire is statistically more precise than along the long axis of an in-plane nanowire (Fig. 3i and Supplementary Note 8), which suggests that the fine tip of a rod-like particle can be used as a vertical 'pen' for high-spatial-resolution probing, sensing and operation.

We further evaluate how small nanoparticles can be manipulated and successfully realize full control of a 300-nm-long Au nanowire (125 nm in diameter) in a glycerol–water mixture (Supplementary Video 3 and Supplementary Notes 9 and 10). The positioning precision reaches 52 ± 10 and 44 ± 6 nm along the long and short axes, respectively. The overall performance is summarized in Table 1.

Active propulsion along complex trajectories

Examples of the combined effect of a.c. and d.c. electric fields on nanowires are shown in Fig. 4a (Supplementary Video 4). Along the entire track, the nanoparticle is positioned with an accuracy of 136 nm (s.d., 110 nm) during transport, and the orientation of the nanowire is

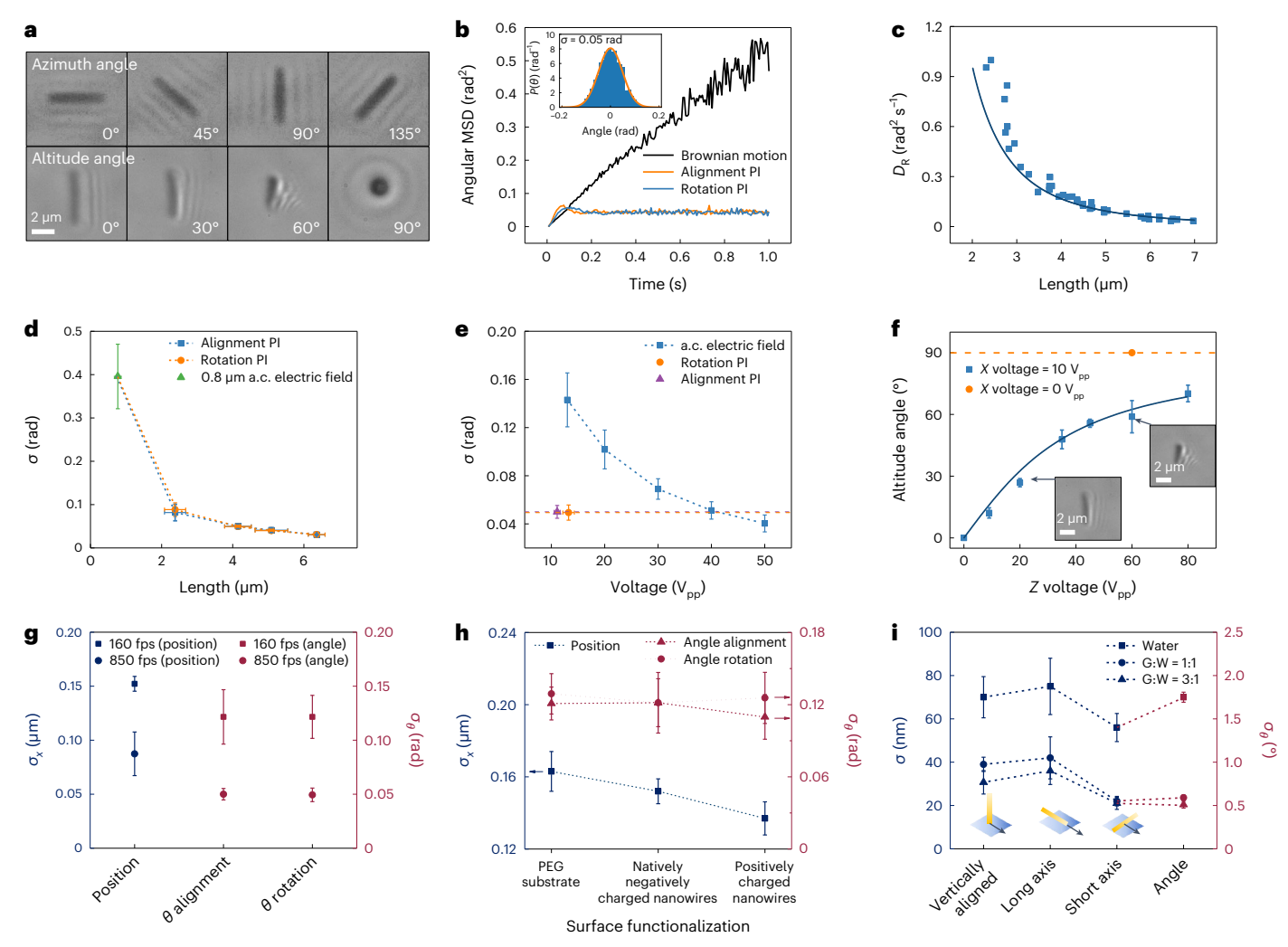


Fig. 3 High-precision angular manipulation and optimization, a. Snapshots of a nanowire aligned at azimuth and altitude angles of 0-135° and 0-90°, respectively. b, Angular MSD of nanowires due to Brownian motion (black), under alignment (orange) and with rotational PI control (blue) versus time. The inset shows the histogram of angle distribution under rotational PI control fitted with a Gaussian distribution (orange), c. Rotational diffusivity of Aunanowires versus length agrees well with the theoretical prediction (solid line) based on the Broersma relation. d, Precision of the angular manipulation under alignment and rotational PI control versus length. The angle control of 0.8 µm nanowires (green) is achieved with a simple linear a.c. electric field at 50 V_{pp} . \mathbf{e} , Directly aligning a nanowire with a linear a.c. electric field requires a much higher voltage compared with rotational (orange) and alignment (purple) PI controls to achieve the same orientation precision (nanowires are 4 μ m in length and 170 nm in diameter). The dashed lines in \mathbf{d} - \mathbf{f} are guides to the eye. \mathbf{f} , Altitude angle versus voltage in the Z direction at 10 V_{pp} (blue) and 0 V_{pp} (orange) in the X direction. The fit (black line) agrees with the experimental studies (Supplementary Note 6). The insets show the top-down microscopy image of the nanowires. g-i, Characterizing and optimizing the manipulation precision. The manipulation precision increases with the video capture rate (160 and 850 fps) (g). Surfacecharge treatment effect (h): low impact to angular precision (red); enhanced

precision in positioning due to increased propelling force via optimizing surface charging (blue). Manipulation precision increases with viscosity of the medium (glycerol-water mixture) for both positioning (blue) and angular (red) control along the in-plane long axis, in-plane short axis and vertical orientations (i). The vertical error bars in \mathbf{d} - \mathbf{i} represent the s.d. values of precision measured for multiple nanowires. The horizontal error bars in **d** and **e** represent the s.d. values of lengths and voltages measured for multiple nanowires, respectively. All data are presented as mean values \pm s.d. Five nanowires are measured to derive the statistics in d and e (rotation PI, alignment PI and a.c. electric field at 20, 30 and 40 V_{pp}, respectively), **f** and **g** (angular precision) and **h** and **i** (long/short axis/ angle in water medium, vertically aligned in a glycerol:water (G:W) = 3:1 medium). In \mathbf{e} , seven nanowires are measured for 13 V_{DD} and eight nanowires are measured for 50 V_{np} . In g, for position control, there are two directions (X and Y) for one nanowire. For 160 fps, the sample size is ten for five nanowires. For 850 fps, the sample size is 12 (for 6 nanowires). In i, six nanowires are measured for vertically aligned position precision in the water medium and for position along the short and long axes in a glycerol:water = 3:1 medium. Eight nanowires are measured for angle control in the glycerol:water = 3:1 medium. Three nanowires are measured for the glycerol:water = 1:1 medium.

controlled by aligning it in the transverse or parallel direction to the tangent of its trajectory, and by rotating it clockwise and anticlockwise at selected points along the trajectory (Supplementary Video 4). The orientation of the nanowire can be maintained at an arbitrary relative angle during the translation, such as at 45° and 135° to the transport direction (47–50 s; Supplementary Video 4). A second trajectory demonstrates in-plane control (large cat in black) and out-of-plane control

(small cat in blue), where the latter is achieved with a vertically aligned nanowire (Supplementary Fig. 5 and Supplementary Video 5). The angular control is further examined for a nanowire in active transport (Supplementary Note 11).

The electrokinetic trap can also manipulate complex functional nanostructures such as a nanopen made of a 50 nm Au tip (diameter, 50.9 ± 23.4 nm) and an Al_2O_3/SiO_2 body shaft with an integrated

Table 1 | Overall performance of the 3D electrokinetic trap

Length (µm)	Medium	$\sigma_{_a}$ (nm)	σ_b (nm)	$\sigma_{\rm v}$ (nm)	σ _θ (°)
6.4	3:1 glycerol:water	36±6	21±3 (best precision, 17)	31±5	0.51
6.4	Deionized water	75±13	56±6	70±9	1.75
0.8	Deionized water	151±22	133±22	-	22.7
0.3	3:1 glycerol:water	52±10	44±6	-	Confirmed alignment

Summary of the achieved precision in the control of nanowires for different experimental conditions. Here σ_a and σ_b are the precisions along the long and short axes, respectively, and σ_v and σ_a are the precision values when the wire is aligned vertically and with angular precision, respectively. The orientation control of the 300-nm-long nanowires is confirmed from the directional anisotropic control precision (Supplementary Note 9).

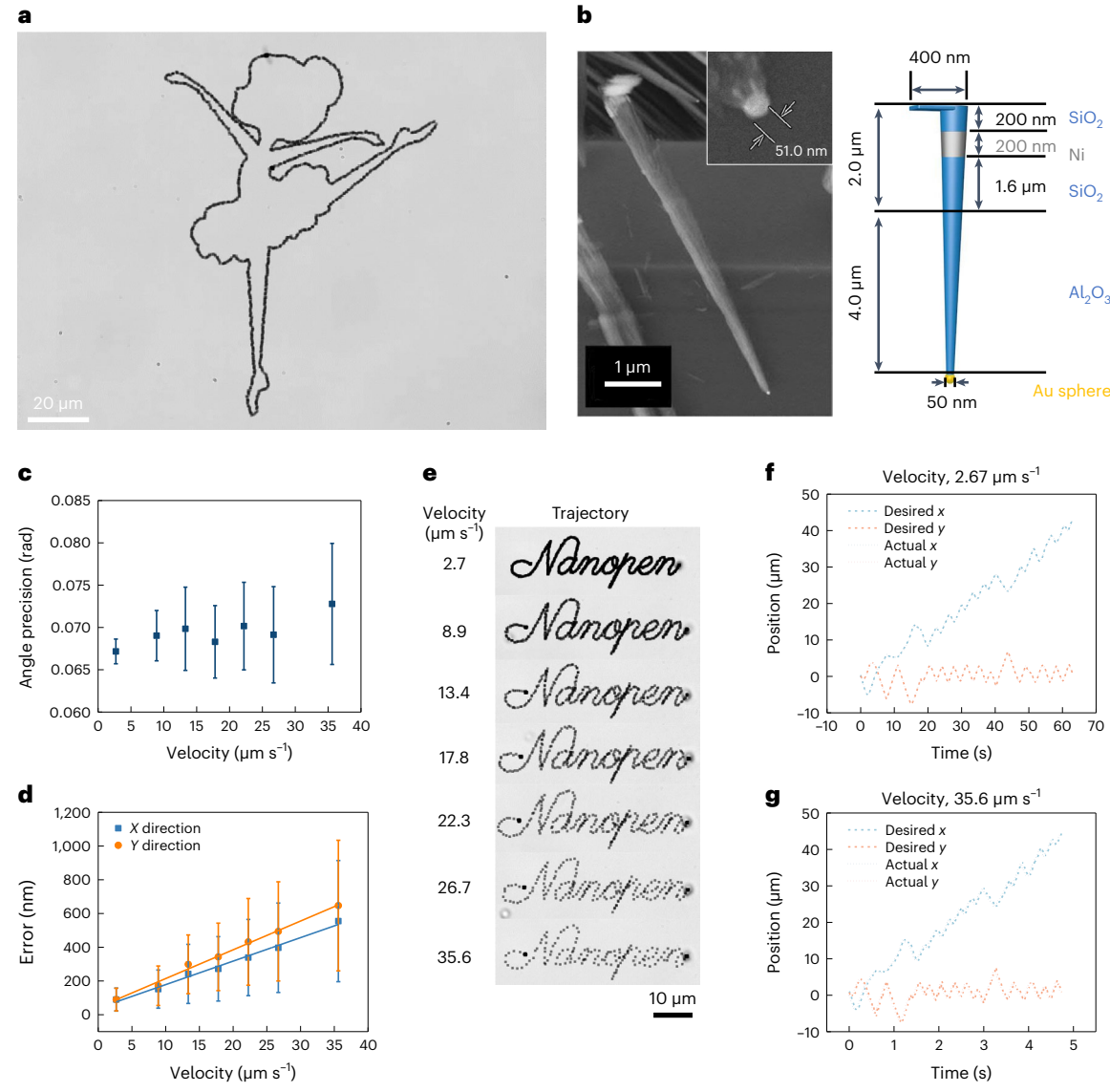


Fig. 4 | **High-precision trajectories with in-plane and out-of-plane control. a**, A nanowire 'writes' the image and translates, rotates and aligns under full computer control. **b**, SEM image and schematic of a nanopen with a 50 nm Au tip and integrated magnetic Ni. **c**, Angular precision versus velocity (single wire). Average of the measurements controlled at 0°, 45° and 90°, each angle for six times; when a wire's long axis is tangential to the trajectory, the angle is defined as 0°. The linear trajectory has a total length of 116 μm. **d**, Manipulation accuracy versus velocity of the propelled vertically oriented nanopen in **b**. The error bar represents the s.d. values of position accuracy for a given speed. **e**, Writing nanopen at 2.7 to 35.6 μm s⁻¹, and the sampling interval is 1/30 s.

f.g. Overlaps of targeted and actual positions versus time at 2.67 μ m s⁻¹ (**f**) and 35.6 μ m s⁻¹(**g**). Data are represented as a single measurement. Supplementary Fig. 8 shows the enlarged images. In **c**, data are represented as mean values \pm s.d. Six measurements from the same nanowire are used to derive the statistics. In **d**, the accuracy is defined by the distance of the attained position/angle from the targeted position/angle during transport, and its mean value is represented by 'error' in the *Y* axis. The error bar at a speed represents the s.d. value of the position accuracy during the transport of the wire. The sample size depends on the duration of trapping. There are 10,678 data points at the speed of 2.7 μ m s⁻¹ and 803 data points at the speed of 35.6 μ m s⁻¹.

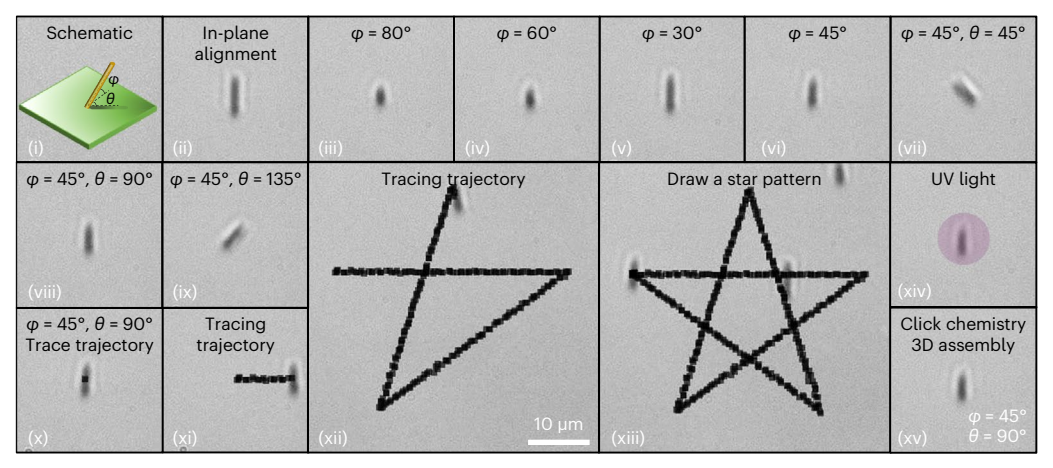


Fig. 5|3D-oriented precision manipulation and assembling. A series of snapshots of nanowires aligned at different altitudes and azimuth angles. A titled nanowire traces a star pattern and is assembled on the substrate on UV illumination and maintains its 3D angle.

Ni magnet (Fig. 4b). The plasmonic Au tip can be heated with light and then penetrates a cell⁴⁹. The Ni segment (Fig. 4b) permits additional magnetic control and is used to ensure that the nanopen always stands up vertically with its Au tip pointing down (Fig. 4e and Supplementary Video 6). The nanopen can transport along complex patterns with an accuracy of 90 nm (s.d., 68 nm) at 2.7 μ m s⁻¹ and 650 nm (s.d., 390 nm) at 35.6 μ m s⁻¹ (Fig. 4d); Supplementary Fig. 6 shows the time-dependent plots. The accuracy of the trace is, however, essentially unaffected (Fig. 4f,g).

Assembly of 3D-oriented nanoparticles

Our technique can also assemble nanostructures with 3D orientation at chosen locations on a substrate, which is useful for electrical or optical applications. As shown in Fig. 5 and Supplementary Video 2, we first move a nanowire (Au) and orient it in a series of programmed altitude angles with a fixed azimuth direction followed by rotating its azimuth angle at a given altitude angle. Next, the nanowire is rapidly moved along a star trajectory (45° in altitude and 90° in azimuth angle), before finally fixing at a target position to the substrate, maintaining its 3D orientation. The assembly is via ultraviolet (UV)-light-triggered click chemistry between its tip and the substrate (Methods). With this approach, 50 Au segments encapsulated in silica are positioned in an array (Supplementary Note 12 and Supplementary Video 7), demonstrating the applicability in the 3D-oriented assembly of nanoparticles.

Nanowire probe scanned across a single bacterial cell

Finally, the electrokinetic trap is used to move a nanowire probe across a bacterial cell and it maintains the position for spectral measurements (Supplementary Note 13). Its plasmonically sensitive body enables the detection of metabolites released by a single bacterial cell. The surface-enhanced Raman scattering (SERS) sensor is an ~800-nm thick SiO₂-coated Au nanorod decorated with ~20 nm Ag nanoparticles. The Ag nanoparticles provide plasmonic signal enhancement for Raman sensing^{50,51}; the diameter of the tip has the approximate width of an Escherichia coli cell⁵². We operate the nanosensors in two modes, that is, actively transport to an *E. coli* cell without mechanical moving parts in the system, and by passive trapping the sensor with electric fields and mechanically moving a fixed *E. coli* cell to the sensor's tip. Both approaches allow the contact of the tip of the plasmonic sensor with the bacterial cell (Supplementary Video 8). As shown in Supplementary Video 9, no Raman signals can be detected at a distance of 20 μm from an E. coli cell. However, on contact, a Raman spectrum is recorded. When the sensor moves 15 µm away from the *E. coli* cell, the Raman signal disappears in time (Fig. 6). The observation agrees with the biochemical release from single live cells, which is known to be localized

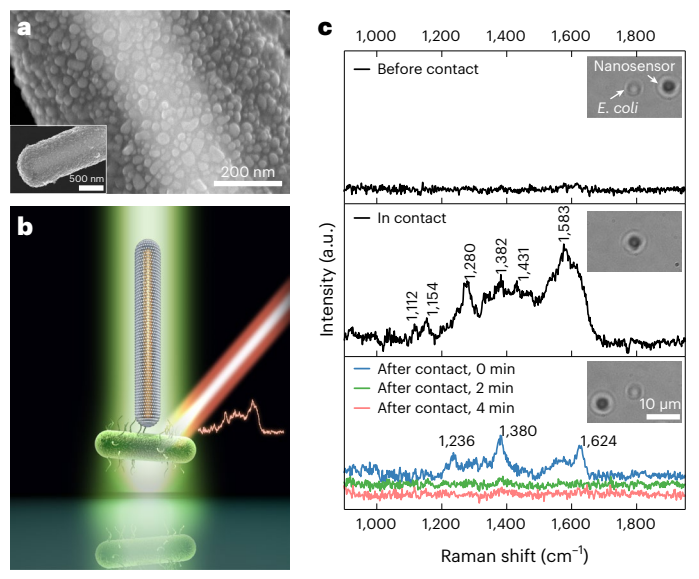


Fig. 6 | Localized detection of metabolites from a single $\it E. coli$ cell with SERS-active nanocapsule sensors. a,b, SEM image (a) and schematic (b) of a vertically aligned silica-encapsulated nanowire with high-density plasmonic Ag nanoparticles on the surface for detecting Raman signals from a single bacterial cell via direct tip contact. c, Raman spectra obtained at 20 μ m distance, in contact and 15 μ m in distance from an $\it E. coli$ cell after contacting. Each Raman spectrum represents a single measurement. The insets show the optical images of the positions of the nanocapsule sensor relative to $\it E. coli$.

within a few cell diameters 3 . The Raman signals are observed to correspond to metabolites released from a single $E.\,coli$ cell, and the spectra suggest that uric acid, xanthine, hypoxanthine, guanine, adenine and adenosine monophosphate are detected (Supplementary Note 14) 54 . The $E.\,coli$ cells are shown not to be affected by the electric fields (Supplementary Note 15).

Conclusions

In summary, we report an electrokinetic trap that permits the simultaneous control of the 3D orientation and 2D position of anisotropic nanoparticles. It can be used to counter translational and rotational Brownian motion and simultaneously steer and orient nanowires actively with exceptional temporal, positional and angular accuracy along complex trajectories. The system can easily operate in two modes, that is, trapping of a particle and active transport. We demonstrate

position control to within 21 ± 3 nm and absolute angles of $0.51\pm0.04^\circ$ in suspension, corresponding to a trap stiffness of 4.3×10^{-6} N m⁻¹ and 5.2×10^{-17} N m rad⁻¹. The system is close to the theoretically predicted precision due to Brownian-motion fluctuations (Supplementary Note 10). The technique controls nanowires as small as 300 nm in length. We successfully propel a nanoprobe such that its plasmonic tip moves in solution across the surface of a bacterial cell and stably positions at a designated location on the bacterium for detection. The nanosensor, thus, provides the means to obtain the location-specific SERS signals of metabolites released from a single *E. coli* cell. The electrokinetic trap requires a 3D microelectrode arrangement and is suitable for on-chip and in vitro applications. It works in ionic (1 mM potassium chloride) and cell culture solutions (Supplementary Note 15).

The performance of the electrokinetic trap reported here favourably compares with other state-of-the-art techniques (Supplementary Table 1) and enables its use as an untethered tool for biospectroscopy. A clear difference to anti-Brownian-motion positioning, for instance, is the achieved precision. The precision we obtain for an untethered micrometre-sized wire with a 50 nm tip is higher than what can be obtained for a 50 nm spherical particle in an anti-Brownian-motion trap. Orientation control has not been shown previously to the level that we have demonstrated here, namely, 0.5° for 6 μ m nanowires. When oriented in three dimensions with 2D positioning control, the nanotip (50 nm) and micrometre-long body provide nanoscale resolution together with an enhanced precision due to the micrometre-scale body that reduces Brownian motion. Supplementary Table 2 shows a quantitative comparison.

Finally, the underlying principles of our electrokinetic trap are generic, and therefore, we expect these results to stimulate further work in micro-/nanorobotics, assembly and micromanipulation, as well as biological measurements with subcellular resolution.

Online content

Any methods, additional references, Nature Portfolio reporting summaries, source data, extended data, supplementary information, acknowledgements, peer review information; details of author contributions and competing interests; and statements of data and code availability are available at https://doi.org/10.1038/s41565-023-01439-7.

References

- Wang, W., Duan, W., Ahmed, S., Mallouk, T. E. & Sen, A. Small power: autonomous nano- and micromotors propelled by self-generated gradients. Nano Today 8, 531-554 (2013).
- Palagi, S. & Fischer, P. Bioinspired microrobots. Nat. Rev. Mater. 3, 113–124 (2018).
- Li, J., Esteban-Fernández de Ávila, B., Gao, W., Zhang, L. & Wang, J. Micro/nanorobots for biomedicine: delivery, surgery, sensing, and detoxification. Sci. Robot. 2, eaam6431 (2017).
- Joh, H. & Fan, D. E. Materials and schemes of multimodal reconfigurable micro/nanomachines and robots: review and perspective. Adv. Mater. 33, 2101965 (2021).
- Kim, K., Guo, J., Liang, Z. & Fan, D. Artificial micro/nanomachines for bioapplications: biochemical delivery and diagnostic sensing. Adv. Funct. Mater. 28, 1705867 (2018).
- Ru, C., Luo, J., Xie, S. & Sun, Y. A review of non-contact microand nano-printing technologies. J. Micromech. Microeng. 24, 053001 (2014).
- Dholakia, K., Drinkwater, B. W. & Ritsch-Marte, M. Comparing acoustic and optical forces for biomedical research. *Nat. Rev. Phys.* 2, 480–491 (2020).
- Liao, P.-H., Tseng, C.-Y., Ke, Z.-Y., Hsieh, C.-L. & Kong, K. V.
 Operando characterization of chemical reactions in single living cells using SERS. Chem. Commun. 56, 4852–4855 (2020).
- Zhao, X. et al. Surface-enhanced Raman scattering optophysiology nanofibers for the detection of heavy metals in single breast cancer cells. ACS Sens. 6, 1649–1662 (2021).

- Ashkin, A., Dziedzic, J. M., Bjorkholm, J. E. & Chu, S. Observation of a single-beam gradient force optical trap for dielectric particles. Opt. Lett. 11, 288–290 (1986).
- Ghosh, S. & Ghosh, A. All optical dynamic nanomanipulation with active colloidal tweezers. Nat. Commun. 10, 4191 (2019).
- 12. Higurashi, E., Sawada, R. & Ito, T. Optically induced angular alignment of trapped birefringent micro-objects by linearly polarized light. *Phys. Rev. E* **59**, 3676–3681 (1999).
- Huang, Y. et al. Three-axis rapid steering of optically propelled micro/nanoparticles. Rev. Sci. Instrum. 80, 063107 (2009).
- Bingelyte, V., Leach, J., Courtial, J. & Padgett, M. J. Optically controlled three-dimensional rotation of microscopic objects. Appl. Phys. Lett. 82, 829–831 (2003).
- Gosse, C. & Croquette, V. Magnetic tweezers: micromanipulation and force measurement at the molecular level. *Biophys. J.* 82, 3314–3329 (2002).
- 16. Ghosh, A. & Fischer, P. Controlled propulsion of artificial magnetic nanostructured propellers. *Nano Lett.* **9**, 2243–2245 (2009).
- 17. Zhang, L. et al. Artificial bacterial flagella: fabrication and magnetic control. *Appl. Phys. Lett.* **94**, 064107 (2009).
- Kummer, M. P. et al. OctoMag: an electromagnetic system for 5-DOF wireless micromanipulation. *IEEE Trans. Rob.* 26, 1006–1017 (2010).
- Zhang, Z., Huang, Y. & Menq, C. H. Actively controlled manipulation of a magnetic microbead using quadrupole magnetic tweezers. *IEEE Trans. Rob.* 26, 531–541 (2010).
- 20. Ghosh, S. & Ghosh, A. Mobile nanotweezers for active colloidal manipulation. *Sci. Robot.* **3**, eaaq0076 (2018).
- 21. Tanyeri, M., Johnson-Chavarria, E. M. & Schroeder, C. M. Hydrodynamic trap for single particles and cells. *Appl. Phys. Lett.* **96**, 224101–224101 (2010).
- Kumar, D., Shenoy, A., Li, S. & Schroeder, C. M. Orientation control and nonlinear trajectory tracking of colloidal particles using microfluidics. *Phys. Rev. Fluids* 4, 114203 (2019).
- 23. Ropp, C. et al. Fabrication of nanoassemblies using flow control. *Nano Lett.* **13**, 3936–3941 (2013).
- 24. Mathai, P. P., Carmichael, P. T., Shapiro, B. A. & Liddle, J. A. Simultaneous positioning and orientation of single nano-wires using flow control. *RSC Adv.* **3**, 2677–2682 (2013).
- Ding, X. et al. On-chip manipulation of single microparticles, cells, and organisms using surface acoustic waves. *Proc. Natl Acad. Sci. USA* 109, 11105–11109 (2012).
- Cao, H. X. et al. Holographic acoustic tweezers for 5-DoF manipulation of nanocarrier clusters toward targeted drug delivery. *Pharmaceutics* 14, 1490 (2022).
- 27. Braun, M. & Cichos, F. Optically controlled thermophoretic trapping of single nano-objects. ACS Nano 7, 11200–11208 (2013).
- Chen, Y. et al. Carbon helical nanorobots capable of cell membrane penetration for single cell targeted SERS bio-sensing and photothermal cancer therapy. Adv. Funct. Mater. 32, 2200600 (2022).
- 29. Ando, J., Fujita, K., Smith, N. I. & Kawata, S. Dynamic SERS imaging of cellular transport pathways with endocytosed gold nanoparticles. *Nano Lett.* **11**, 5344–5348 (2011).
- Fennimore, A. M. et al. Rotational actuators based on carbon nanotubes. Nature 424, 408–410 (2003).
- 31. Fan, D. L., Zhu, F. Q., Cammarata, R. C. & Chien, C. L. Manipulation of nanowires in suspension by a.c. electric fields. *Appl. Phys. Lett.* **85**, 4175–4177 (2004).
- 32. Chang, S. T., Paunov, V. N., Petsev, D. N. & Velev, O. D. Remotely powered self-propelling particles and micropumps based on miniature diodes. *Nat. Mater.* **6**, 235–240 (2007).
- Edwards, B., Engheta, N. & Evoy, S. Electric tweezers: experimental study of positive dielectrophoresis-based positioning and orientation of a nanorod. J. Appl. Phys. 102, 024913 (2007).

- Fan, D. L., Cammarata, R. C. & Chien, C. L. Precision transport and assembling of nanowires in suspension by electric fields. *Appl. Phys. Lett.* 92, 093115 (2008).
- Boymelgreen, A. M., Balli, T., Miloh, T. & Yossifon, G. Active colloids as mobile microelectrodes for unified label-free selective cargo transport. Nat. Commun. 9, 760 (2018).
- Fields Alexander, P. & Cohen Adam, E. Electrokinetic trapping at the one nanometer limit. Proc. Natl Acad. Sci. USA 108, 8937–8942 (2011).
- Cohen, A. E. Control of nanoparticles with arbitrary two-dimensional force fields. *Phys. Rev. Lett.* 94, 118102 (2005).
- Galajda, P. & Ormos, P. Orientation of flat particles in optical tweezers by linearly polarized light. Opt. Express 11, 446–451 (2003).
- 39. Sachs, J., Günther, J.-P., Mark, A. G. & Fischer, P. Chiroptical spectroscopy of a freely diffusing single nanoparticle. *Nat. Commun.* **11**, 4513 (2020).
- Jones, T. B. Electromechanics of Particles (Cambridge Univ. Press, 1995).
- 41. Kim, K., Xu, X., Guo, J. & Fan, D. L. Ultrahigh-speed rotating nanoelectromechanical system devices assembled from nanoscale building blocks. *Nat. Commun.* **5**, 3632 (2014).
- 42. Masliyah, J. H. & Bhattacharjee, S. Electrokinetic and Colloid Transport Phenomena (John Wiley & Sons, 2006).
- 43. Liang, Z. & Fan, D. Visible light-gated reconfigurable rotary actuation of electric nanomotors. *Sci. Adv.* **4**, eaau0981 (2018).
- Liang, Z., Teal, D. & Fan, D. Light programmable micro/ nanomotors with optically tunable in-phase electric polarization. Nat. Commun. 10, 5275 (2019).
- Guo, J., Gallegos, J. J., Tom, A. R. & Fan, D. Electric-field-guided precision manipulation of catalytic nanomotors for cargo delivery and powering nanoelectromechanical devices. ACS Nano 12, 1179–1187 (2018).

- Earnshaw, S. On the nature of molecular forces which regulate the constitution of luminiferous ether. *Trans. Cambridge Philos.* Soc. 7, 97 (1842).
- 47. Han, Y. et al. Brownian motion of an ellipsoid. *Science* **314**, 626–630 (2006).
- 48. Broersma, S. Rotational diffusion constant of a cylindrical particle. *J. Chem. Phys.* **32**, 1626–1631 (1960).
- 49. Maier, C. M. et al. Optical and thermophoretic control of Janus nanopen injection into living cells. *Nano Lett.* **18**, 7935–7941 (2018).
- Xu, X., Kim, K., Li, H. & Fan, D. L. Ordered arrays of Raman nanosensors for ultrasensitive and location predictable biochemical detection. Adv. Mater. 24, 5457–5463 (2012).
- 51. Xu, X., Kim, K. & Fan, D. Tunable release of multiplex biochemicals by plasmonically active rotary nanomotors. *Angew. Chem. Int. Ed.* **54**, 2525–2529 (2015).
- 52. Cooper, S. The constrained hoop: an explanation of the overshoot in cell length during a shift-up of *Escherichia coli*. *J. Bacteriol*. **171**, 5239–5243 (1989).
- 53. Fan, D. et al. Subcellular-resolution delivery of a cytokine through precisely manipulated nanowires. *Nat. Nanotechnol.* **5**, 545–551 (2010).
- Premasiri, W. R. et al. The biochemical origins of the surfaceenhanced Raman spectra of bacteria: a metabolomics profiling by SERS. Anal. Bioanal. Chem. 408, 4631–4647 (2016).

Publisher's note Springer Nature remains neutral with regard to jurisdictional claims in published maps and institutional affiliations.

Springer Nature or its licensor (e.g. a society or other partner) holds exclusive rights to this article under a publishing agreement with the author(s) or other rightsholder(s); author self-archiving of the accepted manuscript version of this article is solely governed by the terms of such publishing agreement and applicable law.

© The Author(s), under exclusive licence to Springer Nature Limited 2023

Methods

Electrokinetic trap and experimental procedure

The experimental realization involves a manipulation system consisting of electrodes made on three layers, that is, an indium tin oxide (ITO) glass and in-plane Au quadruple microelectrodes separated by a PDMS well in the Z direction with another ITO layer deposited at the opposite side of the in-plane microelectrodes (Fig. 1a).

The quadruple microelectrodes are fabricated by standard photolithography using the MICROPOSIT S1811 photoresist (Kayaku Advanced Materials) on the backside of ITO-coated coverslips (22 × 22 mm, thickness #1.5 (0.16–0.19 mm thick), 8–12 Ω ; Structure Probe). A PDMS well with a diameter of 4 mm and a thickness of 1 mm is used to confine the nanoparticle suspension. Another ITO-coated coverslip is placed on top of the PDMS well with the ITO side in contact with the suspension. The entire chip is placed on an inverted microscope (IX71, Olympus) with a $100 \times$ oil-immersion objective (numerical aperture, NA = 1.3). In the pattern-tracking demonstration, a $50 \times$ objective (NA = 0.80) is used; in the Raman sensing experiment, a $20 \times$ objective (NA = 0.45) is used; in the assembly experiment, a $40 \times$ UV objective (LMU-40X-UVB, NA = 0.49; Thorlabs) is used.

In a typical experiment, 13 μ l of the nanoparticle suspension in deionized water is dispersed in the PDMS well. The nanoparticles (for example, Au nanowires, multifunctional nanopens and SERS nanosensors) are well diluted such that particle–particle interactions are not observed.

A complementary metal-oxide-semiconductor camera (acA1300-200 um, Basler) with frame rates of 160 and 850 fps was used for large-area and high-speed imaging, respectively. A customized program based on OpenCV is developed to analyse the images and determine both centre of mass and orientation of a longitudinal nanoparticle by finding a rectangle with the minimum area that bounds the contour of the nanowire followed by executing the PI control algorithm for electric manipulation. A customized function generator provides electric voltages to the chip (Supplementary Note 16). Two function generators (33250A, Agilent) and an amplifier (9200, Tabor Electronics) provide voltages in the Z direction.

PI control algorithm

The program compares the real position/angle and set position/angle for each video frame captured by the complementary metal-oxidesemiconductor camera and calculates the deviation (real value - set value = deviation). A feedback voltage is applied based on the deviation in the form of superimposed d.c. and a.c. voltages. Here the d.c. voltage is used to correct the position deviation based on the combined $electro-osmotic and \, electrophoretic \, effects. \, The \, a.c. \, voltage \, orients \, a$ long nanostructure by electric torque, either through electroalignment or electrorotation. For small nanoparticles with high diffusivities in the Z direction, we use direct electroalignment by applying a constant a.c. voltage along a chosen direction. The torque due to electrorotation is independent of the nanowire angle with respect to the field. Although the torque due to electroalignment is a function of the angle between a particle's long axis and electric-field direction, it is the maximum at 45°. To achieve the highest control efficiency, when using the alignment field, we always apply it along a direction that is 45° from a nanowire's instantaneous angle until it rotates to the desired orientation. The control is based on the PI algorithm. Here the integral term is included to eliminate any steady-state errors. We find that if adding the derivative term, the control becomes unstable, and therefore, it is not included in this work. The coefficients for the proportional term (K_p) and integral term (K_i) are optimized with the Ziegler-Nichols method. The coefficients differ for different particles and experimental conditions.

Fabrication

Fabrication of Au nanowires. The Au nanowires are synthesized by electrodeposition into nanoporous templates (110605 Nuclepore

Track-Etched Membranes with a pore size of $0.1\,\mu m$ (polycarbonate); Whatman) in a three-electrode electrochemical cell. Specifically, we deposit 500 nm Cu by electron-beam evaporation on the backside of a nanopore template, which serves as the working electrode. A Pt wire and a Ag/AgCl (3 M KCl) electrode serve as the counter and reference electrodes, respectively. A constant voltage of -0.9 V (versus Ag/AgCl) is applied to reduce the Au ions in the electrolyte (434 HS RTU, Technic) to metallic Au in the nanopores. The length of the nanowires is controlled by the reaction time and the diameter is determined by the pore size. Etching the Cu film and dissolving the polycarbonate template with chloroform release the nanowires. The Au nanowires are centrifuged and washed three times and stored in deionized water.

Fabrication of nanocapsules. Multisegmented (Au/Ni), nanocapsules are fabricated by electrodeposition into an anodized aluminium oxide template (Anodisc 47, Whatman) using the same three-electrode electrodeposition method discussed above, where Au is deposited at -0.9 V and Ni is deposited at -0.8 V (versus Ag/AgCl). The Au and Ni segments are $1.04 \pm 0.09 \,\mu\text{m}$ and $83 \pm 8 \,\text{nm}$ long, respectively. The average diameter is 296 ± 47 nm. The nanowires are suspended in 0.8 ml deionized water; then, 3 ml ethanol (200 proof, Fisher Chemical), 200 μl tetraethyl orthosilicate (reagent grade, 98%; Sigma-Aldrich) and 50 μl ammonium hydroxide (28-30% solution in water, Fisher Chemical) are mixed in the suspension. After 1 h of sonication, tetraethyl orthosilicate hydrolyses and forms uniform silica shells on the nanowire surface. After washing with deionized water and ethanol alternatively for three times, the Ni segments are etched with nitric acid (Fisher Chemical; diluted three times with deionized water before use) followed by washing and resuspension in deionized water.

Fabrication of SERS-active nanocapsule sensors. The SERS-active nanocapsule sensors made of SiO_2 -coated Au nanowires with surface-distributed Ag nanoparticles are fabricated following the procedure reported elsewhere 50,51,55 . In brief, Au nanowires are fabricated by electrodeposition into an anodized aluminium oxide template (pore size, 300 nm (diameter)) (the 'Fabrication of Au nanowires' section). Then, a SiO_2 layer is coated on each Au nanowire by tetraethyl orthosilicate hydrolysis under sonication (the 'Fabrication of nanocapsules' section). Finally, high-density Ag nanoparticles are synthesized on the silica surface by polyvinylpyrrolidone (M_W , 40,000, CAS 9003-39-8; Sigma-Aldrich)-assisted Ag ion reduction, which provide hot spots for sensitive SERS detection.

Fabrication of nanopens with 50 nm Au tips. The nanopens are fabricated by glancing-angle deposition of SiO₂, Al₂O₃ and Ni on a packed monolayer of 50 nm Au particles covering a Si substrate. The Au particles are prepared by block copolymer micelle nanolithography followed by electroless growth of Au. The block copolymer was dissolved in toluene at a concentration of 4 mg ml⁻¹, and HAuCl₄•3H₂O powder is added to yield self-assembled micelles loaded with HAuCl₄ in their cores. The micelles are then spin coated as a uniform monolayer onto a piranha-cleaned silicon wafer. The wafer is then treated under W10 plasma (350 W, 0.4 mbar) for 45 min to remove the polymer and reduce the metal such that a regular quasi-hexagonal array of 10 nm Au particles forms. The substrate is subsequently immersed in an aqueous solution of 0.1% gold chloride trihydrate and 1 mM hydroxylamine hydrochloride for 30 s, followed by washing with deionized water and drying with nitrogen gas. This step enlarges the diameter of the Au nanoparticles to 50 nm. Another plasma treatment removes the residual polymers. The wafer is transferred to the deposition setup for electron-beam evaporation at a glancing angle of 85°. A 10 nm TiO₂ layer is first deposited on the Au particles as an adhesion layer, followed by 4 μ m Al₂O₃, then by 2 μ m SiO₂ and 200 nm Ni and finally by 200 nm SiO₂. After the substrate is rotated by 180°, 400 nm SiO₂ is deposited to allow the ends of the nanopen (Fig. 4b) to be distinguished in an optical

microscope. To increase electric polarizability for vertical alignment, the nanopens are dispersed on the Si wafer and coated with 5 nm Cr and 10 nm Au by electron-beam evaporation.

Surface functionalization with click chemistry. The substrates (glass with quadruple electrodes) are immersed in 10 mg ml⁻¹ trimethoxysilane-PEG alkyne (M_W , 10,000; Rapp Polymere) solution (95% v/v ethanol and 5% v/v deionized water) with 1% v/v ammonium hydroxide added as a reaction catalyst. After incubating overnight and rinsing with deionized water, they are stored at 4 °C before use.

The silica surface of the multisegment Au capsules (Au@SiO₂) is functionalized following a previously reported procedure ⁵⁶. In brief, the Au@SiO₂ nanocapsules (2×10^7 in 50 µl) are first functionalized in (3-aminopropyl)triethoxysilane (\geq 98.0%, CAS 919-30-2; Sigma-Aldrich), aqueous ammonia and ethanol mixture (at a volume ratio of 10:1:90). After shaking overnight, the nanocapsules are washed with ethanol multiple times and dried in a vacuum under 50 °C for 1 h. Then, 100 µl of 20 mg ml $^{-1}$ HS-PEG-COOH ($M_{\rm w}$, 5,000; Rapp Polymere), 50 µl of 20 mg ml $^{-1}$ N-N'-dicyclohexylcarbodiimide (99%, Sigma-Aldrich) and 50 µl of 12 mg ml $^{-1}$ N-hydroxysuccinimide (98%, Sigma-Aldrich) are dissolved and reacted in dimethyl sulfoxide (anhydrous, Sigma-Aldrich) for 5 h in a glovebox with a nitrogen atmosphere. The mixture is added to the functionalized nanostructures and left to react overnight. The Au capsules are washed with deionized water multiple times and stored in deionized water at 4 °C for future experiments.

For the assembly with UV-triggered click chemistry, a concentration of 2 mg ml $^{-1}$ of 2-hydroxy-4'-(2-hydroxyethoxy)-2-methylpropiophenone photoinitiator (98%, CAS 106797-53-9; Sigma-Aldrich) is added to the functionalized multisegment Au@SiO $_2$ suspension. UV light at 6 mW cm $^{-2}$ is directed through a beam collimator (made of a convex lens (LA4464-UV, Thorlabs), a diaphragm (CP2OS, Thorlabs) and a second convex lens (LA4538-UV, Thorlabs)) to the microscope objective (LMU-40X-UVB, NA = 0.49; Thorlabs). The size of the light spot (-10 μ m) projected via the objective is set with the diaphragm. When a functionalized multisegment Au@SiO $_2$ has been moved into position and oriented with the electrokinetic trap, the UV light is switched on for 10 s to initiate the click reaction that immobilizes the multisegment Au@SiO $_2$ to the substrate.

Raman measurements. Details of *E. coli* are as follows: K-12 strain, living, nutrient broth, catalogue no. 155068, Carolina Biological Supply Company. The *E. coli* cells are washed by repeated centrifugation and resuspension in deionized water. The Raman signals are detected with a Raman microscope (Acton SP2500 spectrometer, Princeton Instruments) excited by a 532 nm laser at 360 μ W after passing through a 20× objective. The exposure time is 1 s and 20 averages have been recorded.

Statistics and reproducibility. The characterizations of positioning and angular precision (Figs. 2 and 3) are statistically obtained by measuring five to eight wires for each data point with the method of s.d. (three nanowires are measured in a glycerol:water = 1:1 mixture; Fig. 3i). Owing to PI control, the averaged position/angle coincides with the targeted position/angle for the non-transporting wires. The positioning/angular precision for each individual nanowire is obtained from more than 6,000 instantaneous position/angle data points collected during its trapping. The control precision of the 0.8 µm nanowires is obtained from the trapped wires for 1.5-5.0 s with a frame rate of 850 fps. Supplementary Fig. 9 shows the noise spectra for the PI and P control of the position and angle with electroalignment and electrorotation, which reflect the oscillatory nature of PI control, beneficial for the coincidence of the averaged position/angle with the targeted position/angle (Figs. 2b and 3b, insets). Multiwire measurements exhibit greater errors compared with single-wire measurement, which can be attributed to their dimensional variation (Supplementary Notes 17 and 18). For single-wire control measurements, additional noise can arise from the instantaneous Brownian motion, changes in local environment and finite observational times limited by the frame rate and pixel size. The imaging measurement method achieves the precisions as shown by the statistical analysis (Supplementary Note 17). No statistical method was used to predetermine the sample size. The sample size was chosen so that it is sufficiently large to ensure statistical significance (Supplementary Notes 8, 9 and 17).

Data availability

All experimental data for the figures in the manuscript are available via Zenodo at https://doi.org/10.5281/zenodo.7765045. Source data are provided with this paper.

Code availability

The codes used for the imaging analysis are available via Zenodo at https://doi.org/10.5281/zenodo.7765045.

References

- 55. Xu, X. et al. Near-field enhanced plasmonic-magnetic bifunctional nanotubes for single cell bioanalysis. *Adv. Funct. Mater.* **23**, 4332–4338 (2013).
- Walker, D., Singh, D. P. & Fischer, P. Capture of 2D microparticle arrays via a UV-triggered thiol-yne 'click' reaction. Adv. Mater. 28, 9846–9850 (2016).

Acknowledgements

This project is supported by the US National Science Foundation (NSF) 1710922 and 1930649 with INTERN, and Welch Foundation F-1734. This project also received partial support from NSF 2219221. H.K. and P.F. acknowledge support from the Max Planck–EPFL Center for Molecular Nanoscience and Technology. We thank B. Lian and S.-I. Hsueh for technical assistance and E. Zumalt for drawing the schematics in Figs. 1 and 6b.

Author contributions

D.F. conceived the concept and approach and supervised the project. H.L. carried out the experiments, data analysis and theoretical calculation, with assistance from D.H. and A.J. D.T. designed and assembled the nanomanipulation system and programmed the software. Z.L. co-developed the system. H.K. and P.F. fabricated the 50-nm-tipped nanopens. H.L., D.F. and P.F. wrote the paper, and all authors confirmed its final form.

Competing interests

The authors declare no competing interests.

Additional information

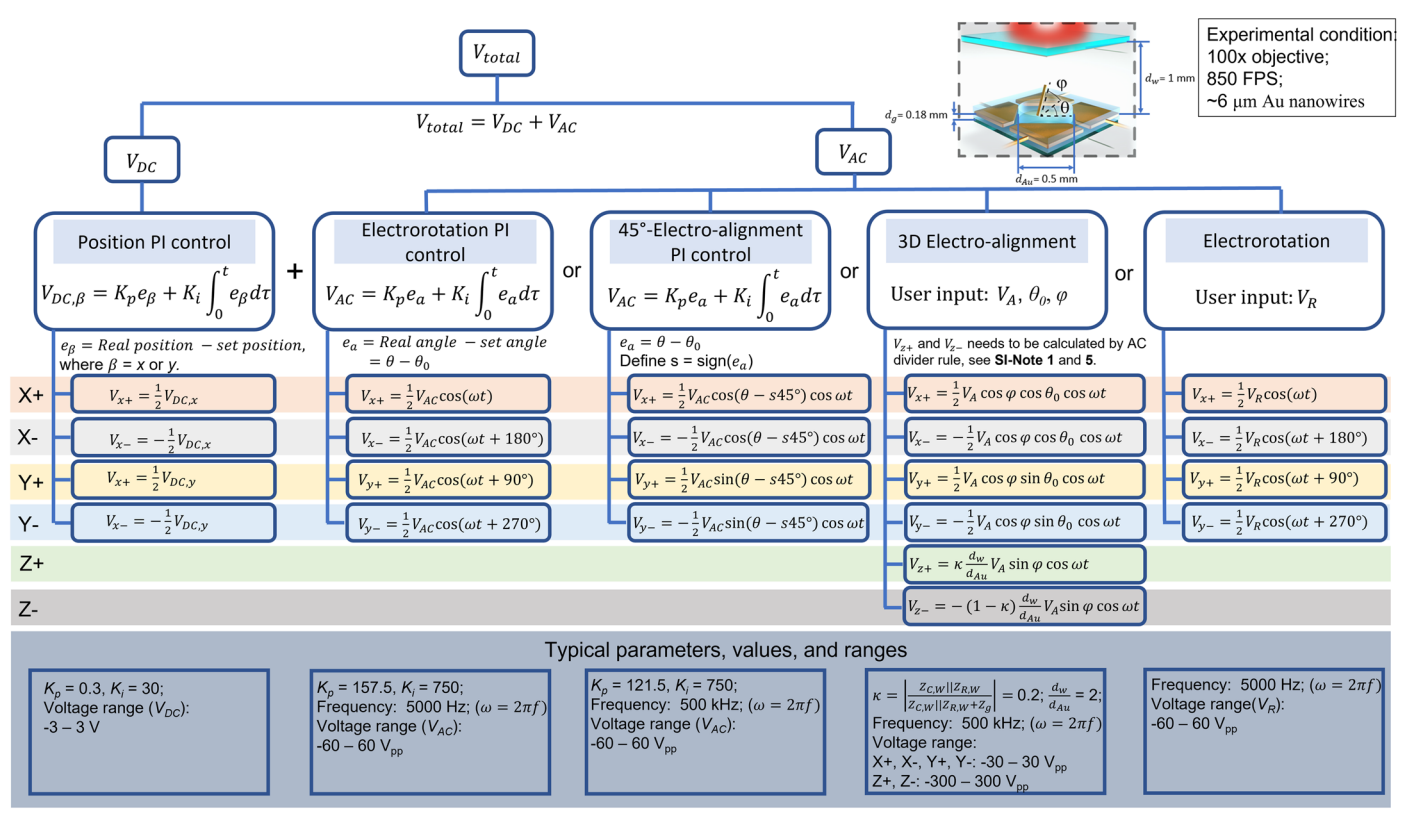
Extended data is available for this paper at https://doi.org/10.1038/s41565-023-01439-7.

Supplementary information The online version contains supplementary material available at https://doi.org/10.1038/s41565-023-01439-7.

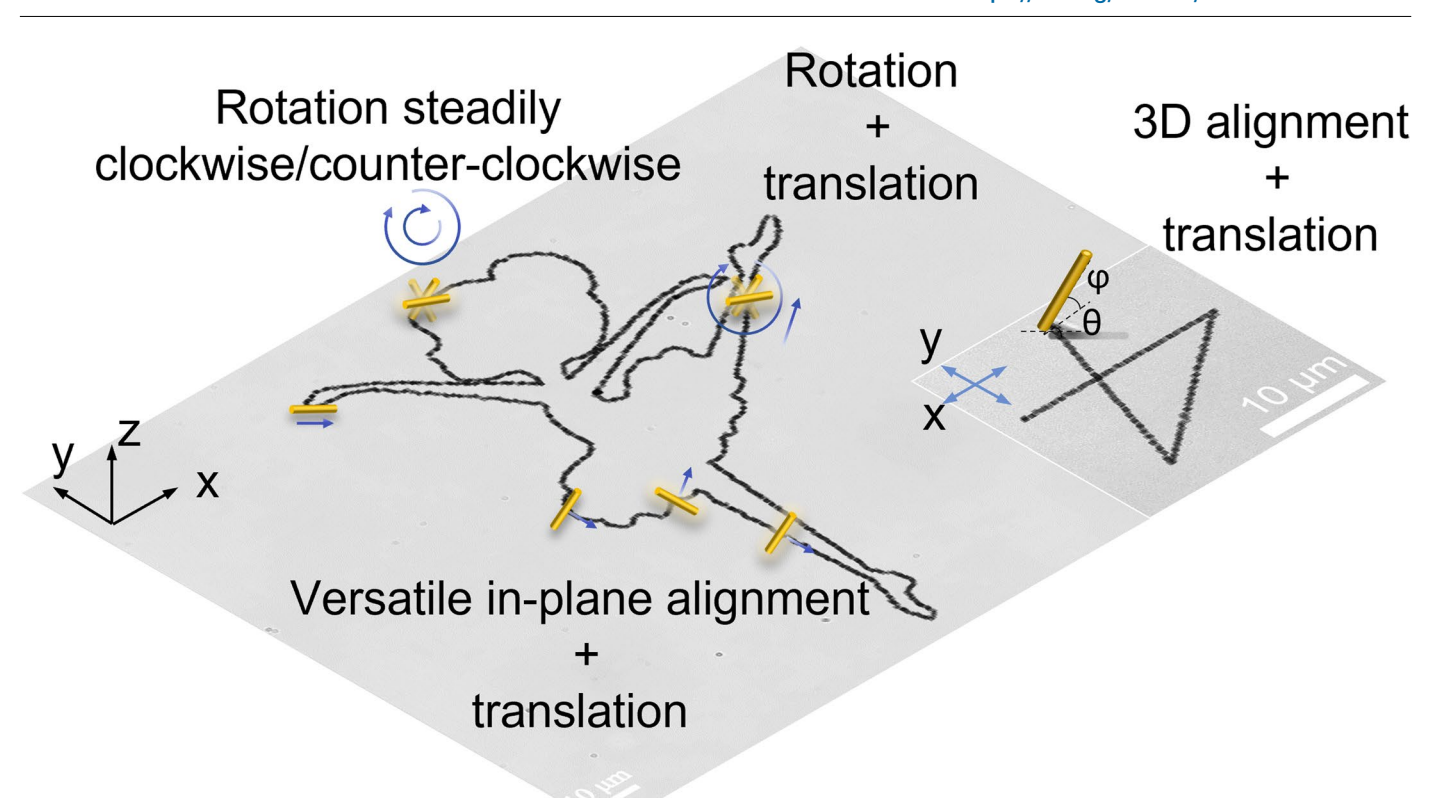
Correspondence and requests for materials should be addressed to Donglei Emma Fan.

Peer review information *Nature Nanotechnology* thanks Natan Osterman and Allison Squires for their contribution to the peer review of this work.

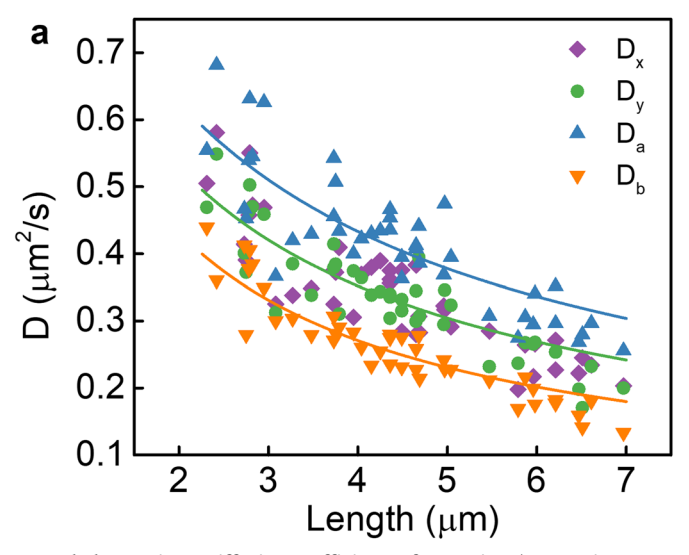
Reprints and permissions information is available at www.nature.com/reprints.

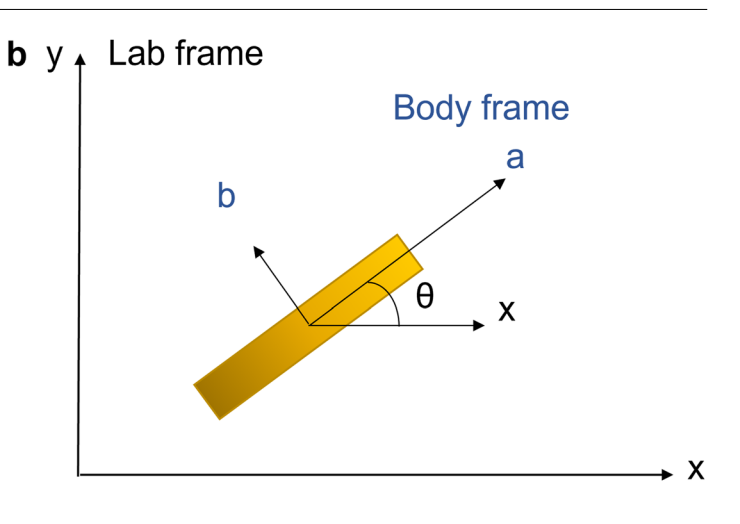


Extended Data Fig. 1 | Electric voltage signals for different control modes. Voltage signals for different control modes.



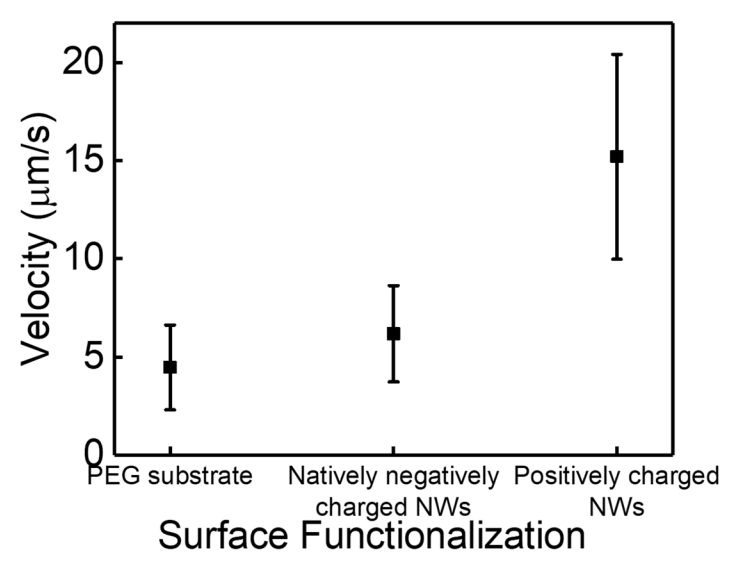
Extended Data Fig. 2 | Schematic shows the synchronous control of position, orientation, and rotation of a nanowire along a sophisticated trajectory with prescribed temporal control. A schematic showing the synchronously executed controls for position, orientation, and rotation of the nanowire along a sophisticated trajectory with precise temporal control.





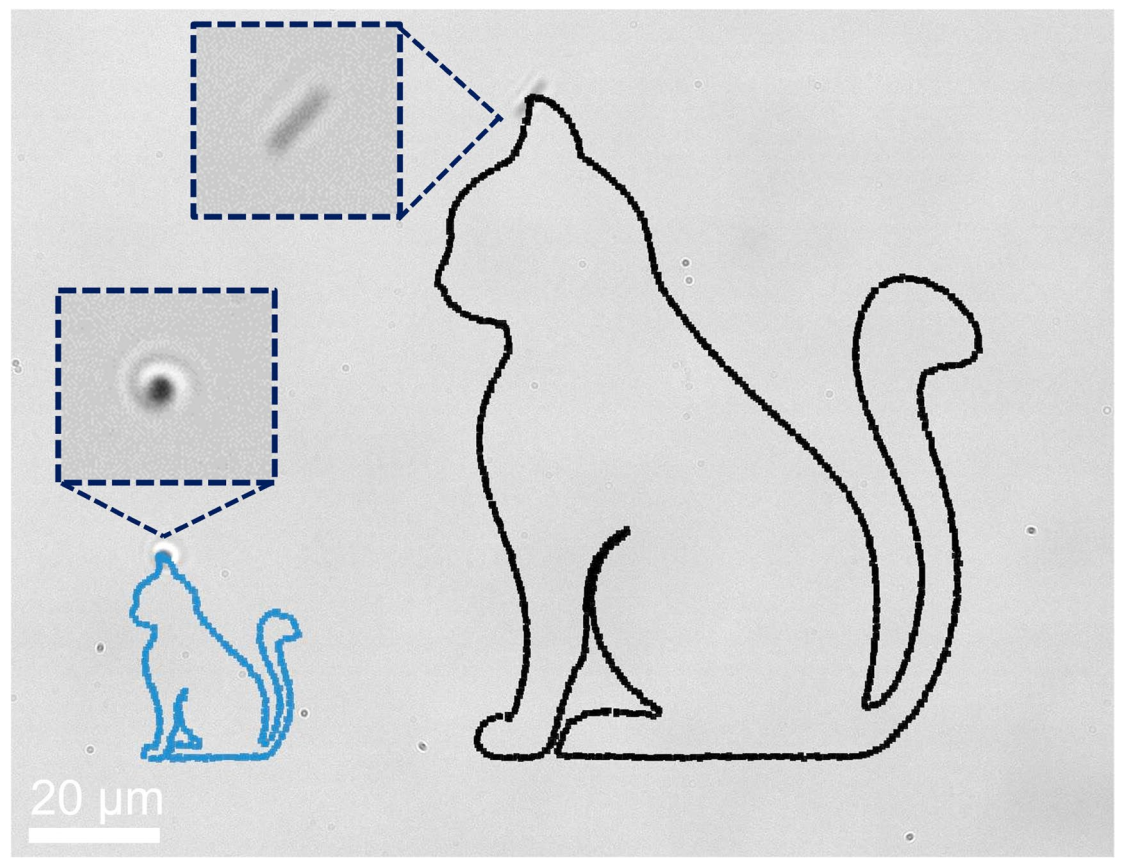
Extended Data Fig. 3 | Diffusion coefficients of nanowires (170 nm in diameter, $-2-7 \mu m$ in lengths) in deionized water along the a, b and x, y orthogonal directions in the body and lab frames, respectively. (a) Diffusion coefficients of nanowires (170 nm in diameter, $-2-7 \mu m$ in lengths) in deionized

water along the orthogonal a, b and x, y directions in the body and lab frames, respectively, in (b). Theoretical fit (solid lines) with the Broersma relation agrees well with experiments; the correction factors (ξ) are 0.883 and 0.801 for translational diffusivities along the long (D_a) and short axis (D_b), respectively.

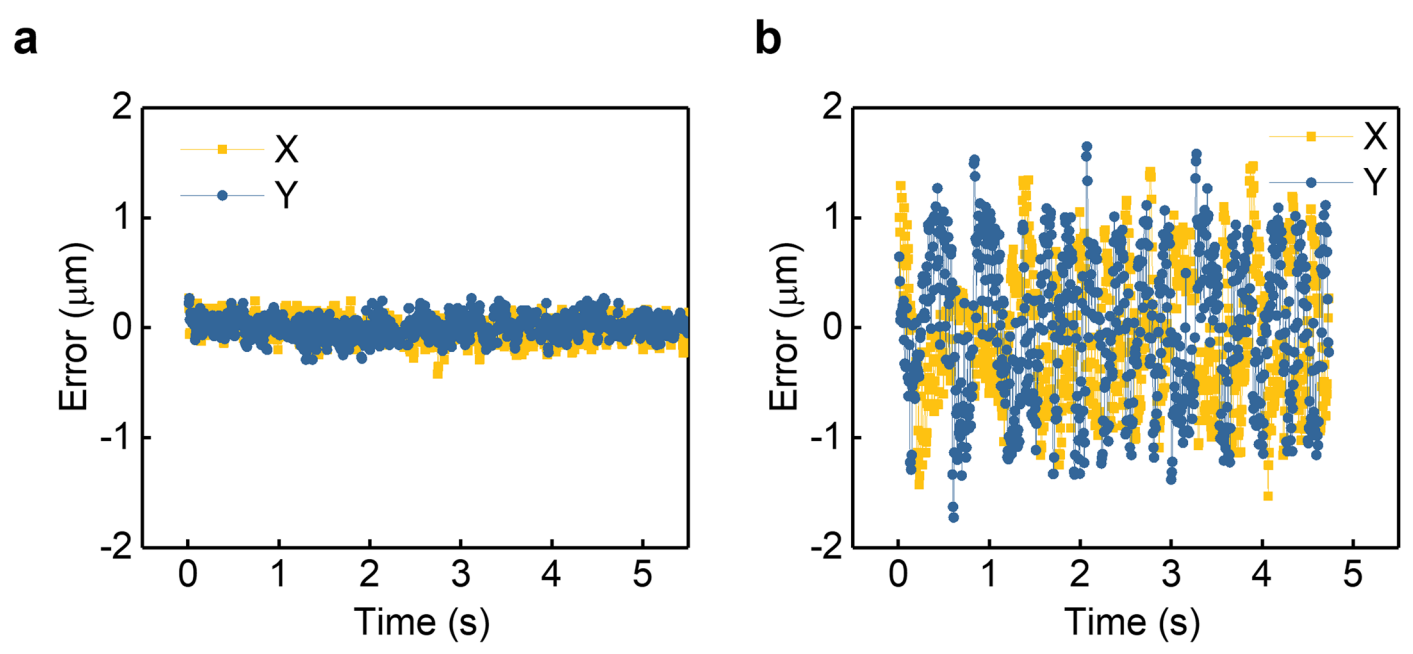


 $\label{lem:extended} \textbf{Data Fig. 4} \ | \ Translational \ velocity \ of \ Au \ nanowires \ on \ different \ surfaces. Translational \ velocity \ of \ Au \ nanowires \ with \ different \ surface \ treatment \ when 1 \ V \ is \ applied \ across \ a 500-\mu m \ electrode \ gap \ (Natively \ negatively \ charged \ NWs, \ zeta \ potential: -40.7 \pm 8.8 \ mV; \ positively \ charged \ NWs, \ zeta \ potential: -40.7 \pm 8.8 \ mV; \ positively \ charged \ NWs, \ zeta \ potential: -40.7 \pm 8.8 \ mV; \ positively \ charged \ NWs, \ zeta \ potential: -40.7 \pm 8.8 \ mV; \ positively \ charged \ NWs, \ zeta \ potential: -40.7 \pm 8.8 \ mV; \ positively \ charged \ NWs, \ zeta \ potential: -40.7 \pm 8.8 \ mV; \ positively \ charged \ NWs, \ zeta \ potential: -40.7 \pm 8.8 \ mV; \ positively \ charged \ NWs, \ zeta \ potential: -40.7 \pm 8.8 \ mV; \ positively \ charged \ NWs, \ zeta \ potential: -40.7 \pm 8.8 \ mV; \ positively \ charged \ NWs, \ zeta \ potential: -40.7 \pm 8.8 \ mV; \ positively \ charged \ NWs, \ zeta \ potential: -40.7 \pm 8.8 \ mV; \ positively \ charged \ NWs, \ zeta \ potential: -40.7 \pm 8.8 \ mV; \ positively \ charged \ NWs, \ zeta \ potential: -40.7 \pm 8.8 \ mV; \ positively \ charged \ NWs, \ zeta \ potential: -40.7 \pm 8.8 \ mV; \ positively \ charged \ NWs, \ zeta \ potential: -40.7 \pm 8.8 \ mV; \ positively \ charged \ NWs, \ potential: -40.7 \pm 8.8 \ mV; \ positively \ positively \ positively \ potential: -40.7 \pm 8.8 \ mV; \ positively \ positively \ positively \ potential: -40.7 \pm 8.8 \ mV; \ positively \ pos$

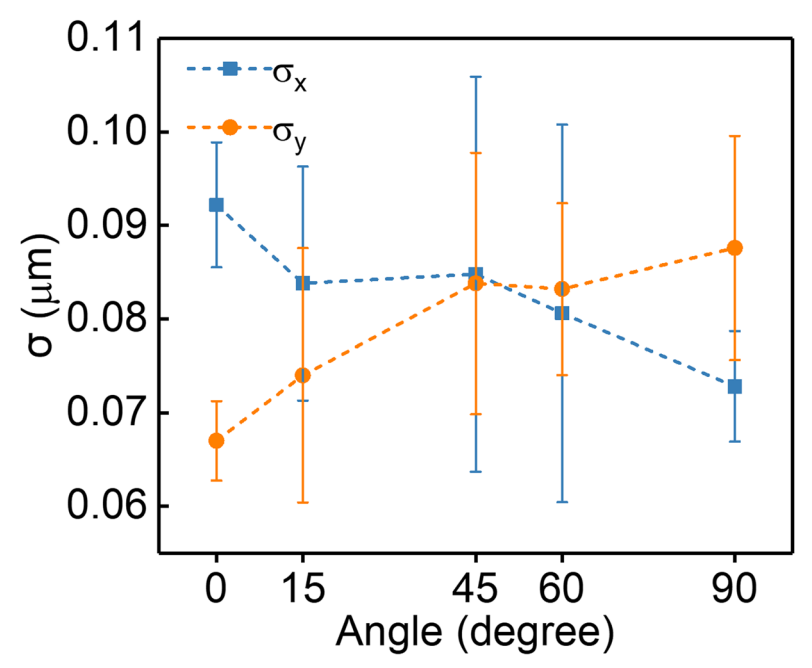
 40.5 ± 4.4 mV.). Data are presented as mean values \pm SD. 20 measurements are made for natively negatively charged NWs, 12 measurements are made for PEG substrate, 20 measurements are made for positively charged NWs.



 $\textbf{Extended Data Fig. 5} | \textbf{Precision manipulation can be readily realized for a wire either in-plane or oriented vertically when it traces a cat pattern.} \ The \textit{precision manipulation can be readily realized in both in-plane tracing and vertical drawing of cat.} \\$

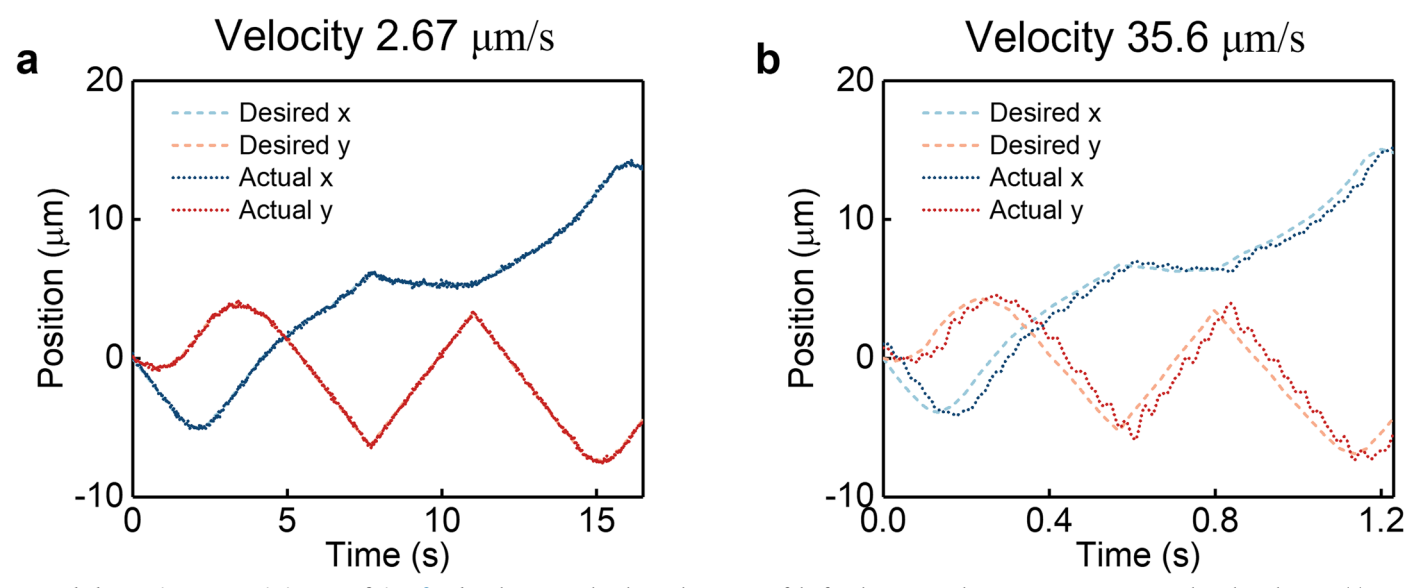


Extended Data Fig. 6 | Position error versus time during the tracing of 'Nanopen' at (a) 2.67 μ m/s and (b) 35.6 μ m/s. Position error versus time as the nanopen traces 'Nanopen' at (a) 2.67 μ m/s and (b) 35.6 μ m/s.

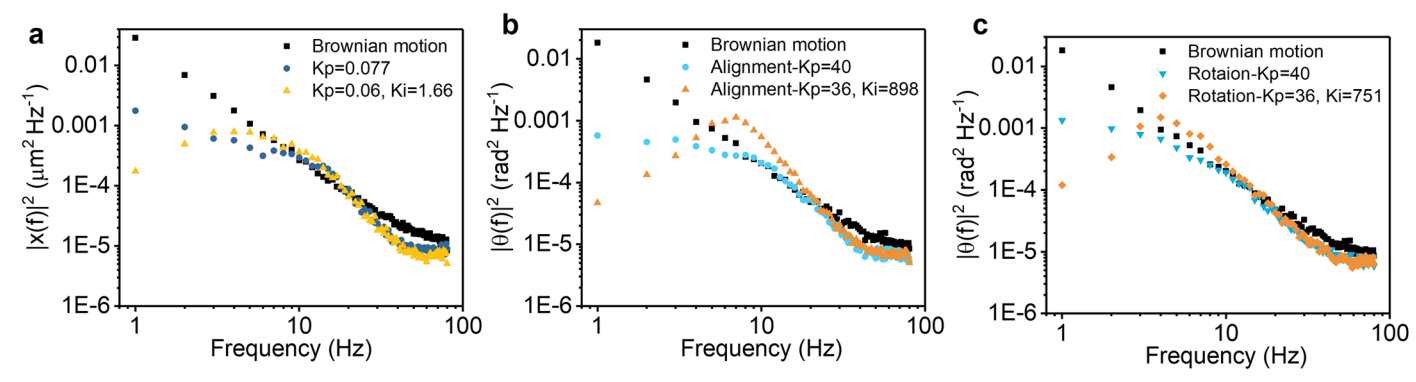


Extended Data Fig. 7 | Positioning manipulation precision of Au nanowires (4- μ m in length) along x (σ_x) and y axis (σ_y), aligned at different angles with a rotational P control (with error bars). Translocation manipulation precision

of Au nanowires (4- μ m in length) along x (σ_x) and y axis (σ_y), aligned at different angles with a rotational P control (with error bars). Data are presented as mean values \pm SD. 5 nanowires are measured to derive statistics.



Extended Data Fig. 8 | Zoom-in images of Fig. 4f and g. The targeted and actual positions of the first letter 'N' in the 'Nanopen' trajectories when the velocity is (a) 2.67 and (b) 35.6 μ m/s.



Extended Data Fig. 9 | Power spectra when particles experience Brownian motion, P control, and PI control for (a) position control, (b) electroalignment angle control, and (c) electro-rotation angle control. The wire length is 4 μ m, the frame rate is 160 FPS. The power spectra of the PI control

(yellow and orange dotted curves) exhibit peaks at around a few Hz, indicating an oscillation. The results agree with the working mechanism of the PI control algorithm, the oscillation of which is intrinsic and benefits the obtained agreement of the average position of the particles with the targeted position.

Extended Data Table 1 | Summary of the performance of the 3D electrokinetic trap

Length (µm)	Medium	$\sigma_{ m a}$ (nm)	σ_{b} (nm)	$\sigma_{_{ m v}}$ (nm)	$\sigma_{ heta}$ (°)
6.4	3:1 Glycerol: water	36 ± 6	21 ± 3 (best precision: 17)	31 ± 5	0.51
6.4	DI water	75 ± 13	56 ± 6	70 ± 9	1.75
0.8	DI water	151 ± 22	133 ± 22	/	22.7
0.3	3:1 Glycerol: water	52 ± 10	44 ± 6	/	Confirmed
					alignment

Summary of the achieved precision in the control of nanowires for different experimental conditions, $\sigma_{\rm s'}$, $\sigma_{\rm b}$ are the precisions along the long and short axis, respectively, $\sigma_{\rm v'}$ and $\sigma_{\rm \theta}$ are the precision when the wire is aligned vertically and the angular precision, respectively. The orientation control of the 300-nm-long nanowires is confirmed from the directional anisotropic control precision (Supplementary Note 9).